

Enhancement of spintronic terahertz emission enabled by increasing Hall angle and interfacial skew scattering

Yangkai Wang^{1,4}, Weiwei Li^{1,4}, Hao Cheng¹, Zheng Liu¹, Zhangzhang Cui^{2,3}, Jun Huang¹, Bing Xiong¹, Jiwen Yang¹, Haoliang Huang^{2,3}, Jianlin Wang^{2,3}, Zhengping Fu^{1,2,3}, Qiuping Huang^{2,3} & Yalin Lu^{1,2,3}

Spintronic terahertz (THz) emitters (STEs) based on magnetic heterostructures have emerged as promising THz sources. However, it is still a challenge to achieve a higher intensity STE to satisfy all kinds of practical applications. Herein, we report a STE based on Pt_{0.93}(MgO)_{0.07}/CoFeB nanofilm by introducing dispersed MgO impurities into Pt, which reaches a 200% intensity compared to Pt/CoFeB and approaches the signal of 500 μm ZnTe crystal under the same pump power. We obtain a smaller spin diffusion length of Pt_{0.93}(MgO)_{0.07} and an increased thickness-dependent spin Hall angle relative to the undoped Pt. We also find that the thickness of a Pt layer leads to a drastic change in the interface role in the spintronic THz emission, suggesting that the underlying mechanism of THz emission enhancement is a combined effect of enhanced bulk spin hall angle and the interfacial skew scattering by MgO impurities. Our findings demonstrate a simple way to realize high-efficiency, stable, advanced spintronic THz devices.

¹Department of Materials Science and Engineering, University of Science and Technology of China, Hefei 230026, P. R. China. ²Hefei National Research Center for Physical Sciences at the Microscale, University of Science and Technology of China, Hefei 230026, P. R. China. ³Anhui Laboratory of Advanced Photon Science and Technology, University of Science and Technology of China, Hefei 230026, P. R. China. ⁴These authors contributed equally: Yangkai Wang, Weiwei Li. ✉email: qphuang@ustc.edu.cn; yllu@ustc.edu.cn

With the advancement of ultrafast laser technology, the THz wave between microwave and infrared gets much attention^{1,2}. The resonance frequencies of various kinds of materials are at the THz band³. THz technology has a wide range of applications due to its unique features, including wireless communications⁴, security⁵, materials characterization^{6,7}, biomedical^{8,9}, spectroscopy, and imaging^{10–12}. The development of THz technology is closely dependent on efficient sources. Traditional THz generation techniques rely on photo-generated electrons in photoconductive antennas^{13,14} and the optical rectification effect^{15,16} of non-linear crystals, such as ZnTe¹⁷, GaP¹⁸, LiNbO₃¹⁹ crystals but the bandwidth of the THz waves generated through these methods is limited due to phonon absorption and phase matching. The rise of spintronics has led to a type of spintronics-based terahertz emitter called spintronic terahertz emitters (STEs)^{20–22}. Typical STEs are based on ferromagnetic/non-magnetic (FM/NM) metallic bilayers, that can convert the spin-polarized currents into transient charge currents via the inverse spin Hall effect (ISHE) or inverse Rashba-Edelstein effect (IREE) and radiate THz waves under the excitation of a femtosecond laser pulse^{23–25}. STEs have the advantages of low cost, ultrathin film, broadband, and optional pumping wavelength, which make STEs promising THz sources, especially for on-chip sources. In recent years, STEs have been studied extensively aiming to obtain stronger signals and wider bandwidths, such as different material compositions and geometrical stacking of FM/NM layers with a variety of thicknesses^{26–28}, interface engineering of FM/NM interface²⁹, coupling of different mechanisms³⁰, and special patterns³¹. Although various strategies have been adopted to improve the THz signal, there is still a great demand for obtaining higher intensity to satisfy the practical application of ultrafast coherent control over the electron spins³², the motion of lattice ions³³ and the transport of charge carriers, even across the atomic-scale junction of scanning tunneling microscopes³⁴.

In STEs, the spin Hall angle can quantify the conversion efficiency of spin current into charge current via ISHE. Pt, W, Ta, and other common 5d heavy metals are frequently utilized as non-magnetic layers for STEs due to their large spin Hall angle^{35–37}. Other materials also have been investigated to replace heavy metals with non-magnetic layers like antiferromagnets³⁸, semiconductors³⁹, and topological insulators (TI)^{40,41} like BiSe and BiTe. Although the TI materials have large spin Hall angles, they exhibit low efficiency in THz emission due to the spin-to-charge conversion (SCC) via IREE being restricted to the surface of TI. Therefore, finding materials with larger spin Hall angles and higher SCC efficiency has become one of the effective methods to improve the emission intensity of STEs.

There have been reports on the possibility of increasing the spin Hall angle of non-magnetic metals by alloying or introducing impurities into the heavy metal materials, such as the enhancement of the spin Hall effect in AuPt⁴², CuPt⁴³, PtAl⁴⁴, and the enhanced spin Hall angle of Pt by introducing MgO⁴⁵, TiO₂⁴⁶ into Pt to form dirty metals. However, these studies focus on the low-frequency properties of materials using electrical methods such as ferromagnetic resonance and spin Hall measurement. In contrast, terahertz emission spectroscopy can also study these doped and alloyed metals with large spin Hall angles. Actually, the employment of enhancing spin Hall angle of heavy metal by doping can provide a great chance to obtain an enhanced spintronic terahertz emission in a simple FM/NM bilayer structure. On the other hand, T. Kampfrath et al. found interfacial skew scattering⁴⁷, an interfacial spin-charge conversion mechanism. Impurities introduced not only remain in the bulk of the metal but may also exist in the interface of FM/NM layers, which likely enhances the effect of interfacial skew scattering⁴⁷ and increases the SCC efficiency. Therefore, to obtain a high-intensity STE,

further mechanism about the spin Hall effect in the doped heavy metals still needs to be understood clearly.

In this article, we propose a high-intensity STE with a simple FM/NM bilayer structure by introducing MgO impurities into the NM heavy metal Pt, aiming at modifying the bulk spin angle and the interface conditions and thus raising the SCC efficiency. We deposited Pt_{0.93}(MgO)_{0.07}/CoFeB nanofilm heterostructures and successfully achieved an enhancement of 100% relative to the standard Pt/CoFeB structure, which reached the signal strength of commercial ZnTe crystals under the same pump power. Moreover, the spin-diffusion length (2 ± 0.2 nm) of Pt_{0.93}(MgO)_{0.07} and thickness-dependent relative spin Hall angle concerning Pt were obtained by fitting the experimental data. Introducing MgO intersite impurities reduces the spin diffusion length but increases the bulk spin Hall angle (originates from the increase in resistance). Furthermore, interlayer investigation on THz emission further elucidates that the underlying enhancement mechanism is a combined effect of increasing bulk spin Hall angle and interfacial skew scattering. Our finding not only achieves a high-efficient THz source but also reveals the non-negligible role of interfaces in the ISHE.

Results

Enhanced THz emission from Pt_{1-x}(MgO)_x/CoFeB heterostructure. Figure 1a is a schematic diagram of our spintronic terahertz emitter for terahertz emission measurement, with the experimental setup as shown in Supplementary Note 1. The x-ray diffraction (XRD) $\theta-2\theta$ patterns of Pt_{1-x}(MgO)_x single layer are shown in Fig. 1b. The typical fcc (111) diffraction peak of Pt is observed. With the increase of MgO doping content, the Pt (111) peak becomes weaker and broader, showing the reduction of Pt atomic ratio. However, the position of the peak almost does not shift, indicating that the MgO exists in the form of interstitial impurities in Pt and does not destroy the long-range order of Pt. To investigate the valence state of Pt and the sample composed of Pt, Mg, and O in Pt_{1-x}(MgO)_x, we performed x-ray photoemission spectroscopy (XPS) measurement on Pt_{1-x}(MgO)_x. The 4f^{7/2} and 4f^{5/2} peaks of Pt are shown in Fig. 1c. Obviously, the 4f^{7/2} and 4f^{5/2} peaks in pure Pt and Pt_{1-x}(MgO)_x are almost unshifted, both at 71.1 and 74.4 eV, respectively^{48,49}. Meanwhile, that Mg 1s and O 1s peaks of the sample are located at 1303.9 and 532.1 eV [Supplementary Note 2], which are in agreement with 1303.9 and 532.1 eV for MgO^{50,51}. Therefore, we believe that Pt is not oxidized in Pt_{1-x}(MgO)_x, while MgO exists in the molecular form. Figure 1d illustrates cross-sectional energy dispersive x-ray spectroscopy (EDS) Pt, Mg, and O mapping of the stack of Pt_{0.93}(MgO)_{0.07}(5)/CoFeB(4)/MgO(1.5) (numbers are thickness in nanometers) under the high-angle annular dark field scanning transmission electron microscopy (HAADF-STEM) mode. We can find that MgO molecules are well dispersed in the Pt layer without obvious aggregation. A cross-sectional transmission electron microscopy (TEM) image is presented in Fig. 1e, indicating that Pt_{1-x}(MgO)_x layer has a polycrystalline and amorphous mixed texture. The atomic force microscopy (AFM) measurement and the CoFeB magnetization for these stacks with different MgO concentrations as shown in Supplementary Note 3 and Supplementary Note 4, respectively. Figure 1f illustrates the typical THz waveform of the SiO₂/Pt_{1-x}(MgO)_x(3)/CoFeB(4)/MgO(1.5) multilayer film with different MgO content ($x = 0, 0.02, 0.05, 0.06, 0.07, 0.13$, respectively), under the same experiment condition. The shape of the THz pulses stayed constant when different MgO concentrations were doped into Pt. In contrast, the peak amplitude of the THz signal decreased first and subsequently increased, reaching its maximum amplitude at $x = 0.07$. Then we grew the structure Pt_{0.93}(MgO)_{0.07}(3)/CoFeB(4) on a 10×10 mm² SiO₂ substrate and

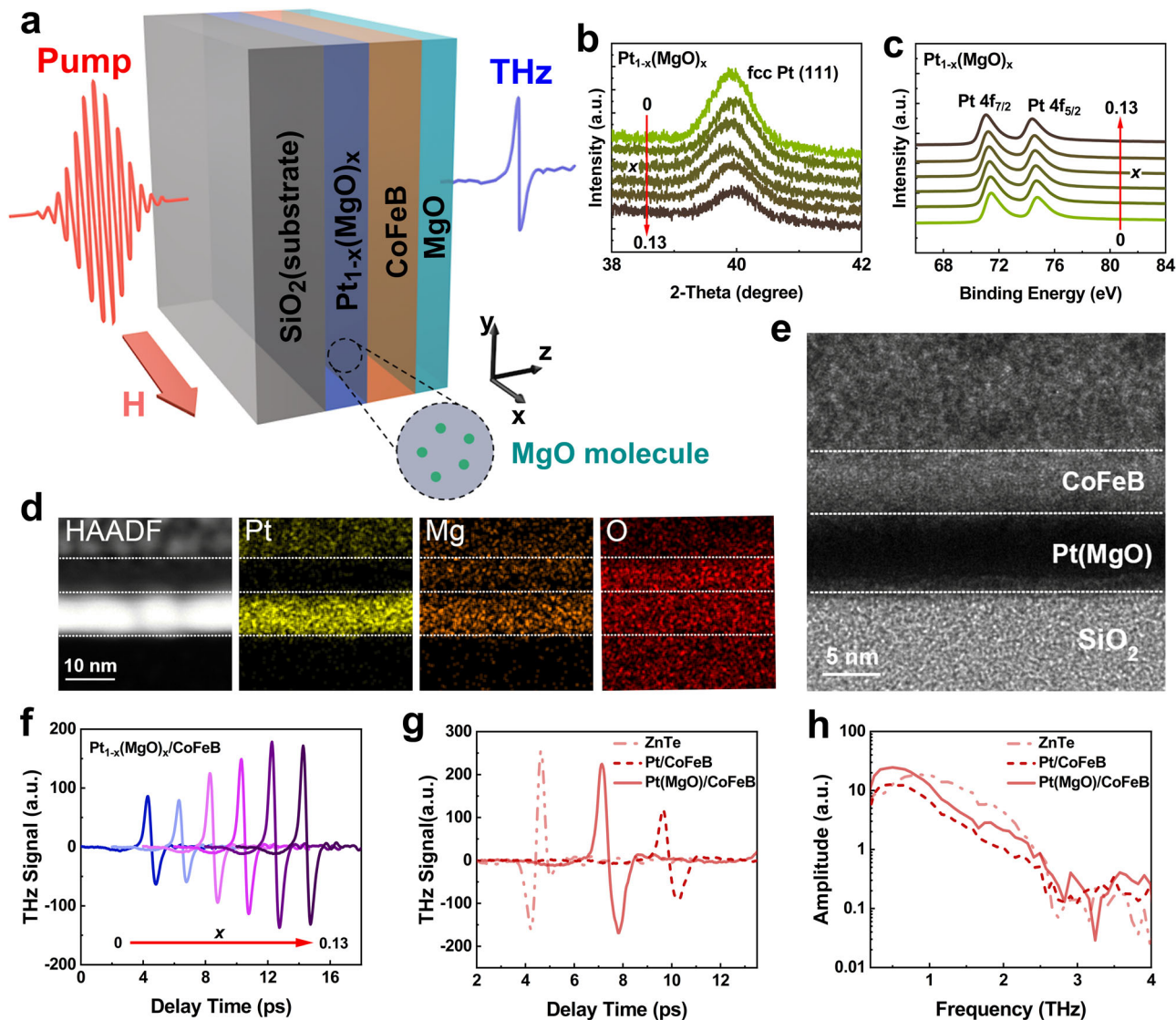


Fig. 1 Sample structure and enhanced THz emission of $\text{Pt}_{1-x}(\text{MgO})_x/\text{CoFeB}$ heterostructures. **a** Schematic diagram of our spintronic terahertz emitter in the experiment, with femtosecond laser incident from the substrate side along the z -direction and the applied magnetic field along the x -direction. **b** XRD θ - 2θ patterns for $\text{Pt}_{1-x}(\text{MgO})_x$ single layer with different x . **c** X-ray photoemission spectroscopy (XPS) for Pt 4f peaks in a $\text{Pt}_{0.93}(\text{MgO})_{0.07}$ single layer. **d** Cross-sectional high-angle annular dark field scanning transmission electron microscopy (HAADF-STEM) image and energy-dispersive x-ray spectroscopy (EDS) mapping of Pt, Mg, and O. The white line in the lower left corner is the scale, and the length of the white line corresponds to the actual length of 10 nm. **e** Cross-sectional high-resolution transmission electron microscopy image of a magnetic stack of $\text{Pt}_{0.93}(\text{MgO})_{0.07}(5)/\text{CoFeB}(4)/\text{MgO}(1.5)$. The white line in the lower left corner is the scale, and the length of the white line corresponds to the actual length of 10 nm. **f** THz waveforms generated by $\text{Pt}_{1-x}(\text{MgO})_x(3)/\text{CoFeB}(4)$ structure with different MgO content. **g** Comparison between the time-domain THz signal from the $\text{Pt}_{0.93}(\text{MgO})_{0.07}(3)/\text{CoFeB}(4)$ (solid red line), $\text{Pt}(3)/\text{CoFeB}(4)$ (deep red dotted line) and that from the ZnTe crystal (light red dash-dot line), at the same pump power. **h** Fourier spectra obtained from the $\text{Pt}_{0.93}(\text{MgO})_{0.07}(3)/\text{CoFeB}(4)$ (solid red line), $\text{Pt}(3)/\text{CoFeB}(4)$ (deep red dotted line) and ZnTe crystal (light red dash-dot line). The data in **f** are shifted horizontally for clarity.

compared its THz signal with $\text{Pt}(3)/\text{CoFeB}(4)$ stack and a commercial 500- μm -thick $10 \times 10 \text{ mm}^2$ ZnTe crystal (Fig. 1g), finding that the signal of the STE could reach 200% of $\text{Pt}(3)/\text{CoFeB}(4)$ stack and 90% of the ZnTe crystal at the same pump fluence ($720 \mu\text{J cm}^{-2}$). Figure 1h shows the Fourier spectra of the THz signal, where the bandwidth is limited by the detection crystal.

For better research on the enhancement of MgO doping on THz emission, we performed further experiments for the stack of $\text{Pt}_{0.93}(\text{MgO})_{0.07}(3)/\text{CoFeB}(4)$ (doped sample) and $\text{Pt}(3)/\text{CoFeB}(4)$ (reference sample). The THz signal emitted from $\text{Pt}_{0.93}(\text{MgO})_{0.07}(3)/\text{CoFeB}(4)$ under different magnetic field directions is shown in Fig. 2a. The phase of the THz wave undergoes a 180° shift when the direction of the magnetic field is reversed. Furthermore, the incident

direction of the pump laser also plays a role in determining the phase of THz radiation. Figure 2b shows the pump fluence dependence of THz signal amplitude. The THz signal amplitude of the reference sample and the doped sample shows the same relationship with incident pump fluence. As the pump fluence increases, the signal grows approximately linearly in the low fluence domain and nonlinearly in the high fluence domain. However, both samples approach a saturated value above the same pump fluence of $\sim 1800 \mu\text{J cm}^{-2}$, indicating that MgO doping does not affect the saturation laser threshold of the sample. The signal of the doped sample is twice as high as that of the reference sample over the entire fluence range, showing that the enhancement effect is stable and independent of the pump fluence.

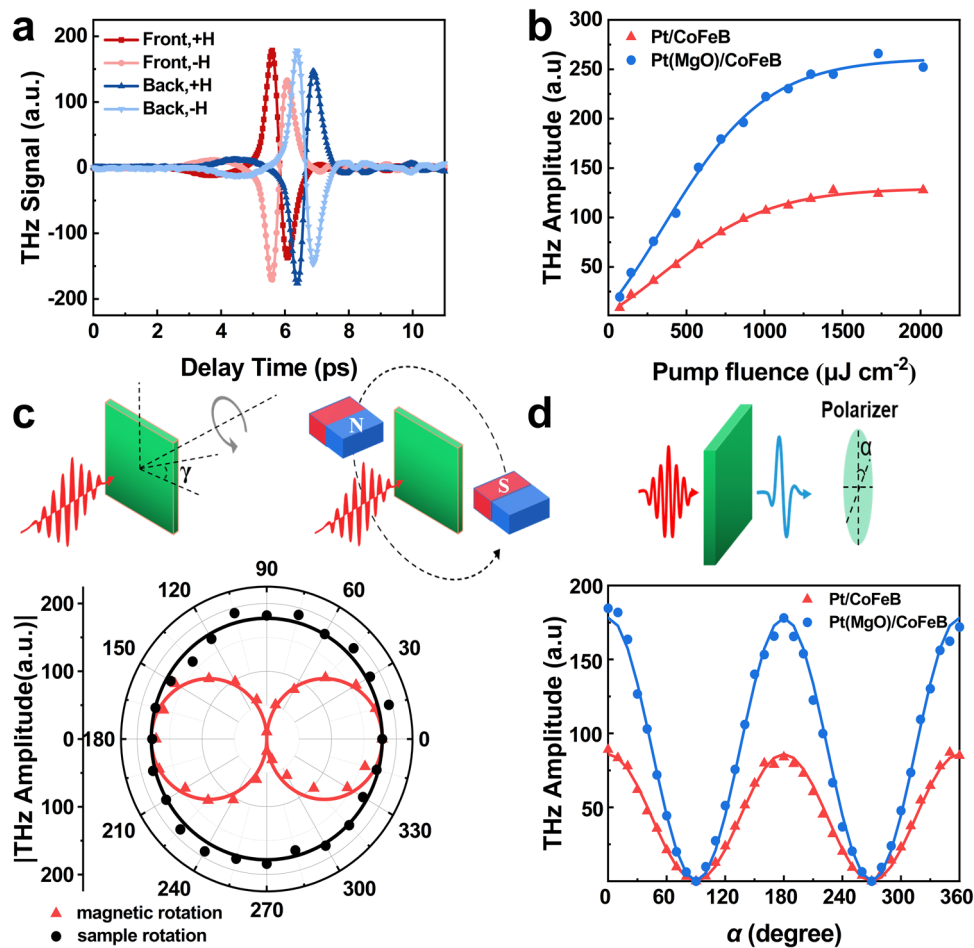


Fig. 2 THz radiation from $\text{Pt}_{0.93}(\text{MgO})_{0.07}/\text{CoFeB}$ heterostructure. **a** Magnetic field directions dependence and laser incident directions dependence of $\text{Pt}_{0.93}(\text{MgO})_{0.07}(3)/\text{CoFeB}(4)$ sample. The red squares represent excitation on the side of the substrate (front) and x-direction magnetic field. Light red circles represent excitation on the side of the substrate (front) and -x-direction magnetic field. Blue up arrows represent excitation on the side of the films (back) and x-direction magnetic field. Light blue down arrows represent excitation on the side of the films (back) and -x-direction magnetic field. **b** Terahertz amplitudes of Pt/CoFeB (blue circles) and $\text{Pt}_{0.93}(\text{MgO})_{0.07}/\text{CoFeB}$ (red triangles) under different pump fluence. The solid lines represent fitting results. **c** THz amplitude as a function of the sample rotation angle γ (black circles) and magnetic field rotation angle β (red triangles). The red line is a constant fit. The black line is a curve fit proportional to $|\cos\gamma|$. **d** Relationship between terahertz amplitude and polarizer rotation angle of Pt/CoFeB (blue circles) and $\text{Pt}_{0.93}(\text{MgO})_{0.07}/\text{CoFeB}$ (red triangles). Solid lines are curve fit proportional to $|\cos 2\alpha|$.

We fixed the position and angle of the doped sample while rotating the magnetic field direction. Figure 2c depicts the signal amplitude as a function of magnetic field angle (β) and the function $E_{\text{THz}} \propto \cos\beta$ best fits the experimental data. We fixed the magnetic field along the x-axis in another experiment and rotated the doped sample's azimuth. Figure 2c shows that the THz amplitude is nearly consistent regardless of the rotation angle (γ). This isotropic behavior implies that the THz enhancement is unaffected by anisotropy in the films. Figure 2d demonstrates the variation in THz amplitude caused by adjusting the angle (α) of the polarizer behind the sample. The experimental data are well fitted by the $E_{\text{THz}} \propto E_0 \cos^2\alpha$ (E_0 is the THz amplitude at $\alpha = 0$). The THz emission behavior exhibited by the doped samples reveals that SCC still plays a key role in THz enhancement without coupling other mechanisms.

The SCC in traditional FM/NM heterostructure is usually ascribed to the ISHE or IREE. IREE usually appears in symmetry-breaking crystals or at special interfaces of thin films⁵². Therefore, we can determine that ISHE dominates the SCC in our experiment. Pump laser pulses excite the FM/NM heterostructure to generate the non-equilibrium carriers and then form a spin current (j_s) flowing toward the z-direction with its spin

polarization parallel to the magnetization (\mathbf{M}) direction from FM to NM. The longitudinal spin currents are transformed into the transverse transient charge currents ($J_C \propto \theta_{\text{SHE}} j_s \times \mathbf{M}$, where θ_{SHE} represents the spin Hall angle for heavy metals, \mathbf{M} denotes the magnetization of FM) due to the strong spin-orbit coupling in NM. All of the processes result in THz emission.

Spin Hall angle and spin diffusion length of $\text{Pt}_{1-x}(\text{MgO})_x$. In order to investigate the underlying physics in the MgO doping enhanced THz emission process, we grew the stacks with different layer thicknesses of Pt and $\text{Pt}_{0.93}(\text{MgO})_{0.07}$ and fixed layer thickness of CoFeB at 4 nm (4 nm which is thicker than the dead layer and the signal from 4 nm CoFeB is negligible, the film thickness dependence of the THz signal for CoFeB is shown in Supplementary Note 5). THz pulse is obtained in all samples as shown in Fig. 3a, b. As the increase of $\text{Pt}_{0.93}(\text{MgO})_{0.07}$ thickness, the THz amplitude experiences a considerable increase firstly and then, a smooth decrease after $t_{\text{Pt}(\text{MgO})} = 3$ nm (Pt(MgO) appearing later in the article represents $\text{Pt}_{0.93}(\text{MgO})_{0.07}$). The maximum value of the THz signal is reached at $t_{\text{Pt}(\text{MgO})} = 3$ nm. The trend of the THz signal variation with the layer thickness of Pt is similar to the doped sample, but the signal of Pt(t)/CoFeB(4) stack reaches

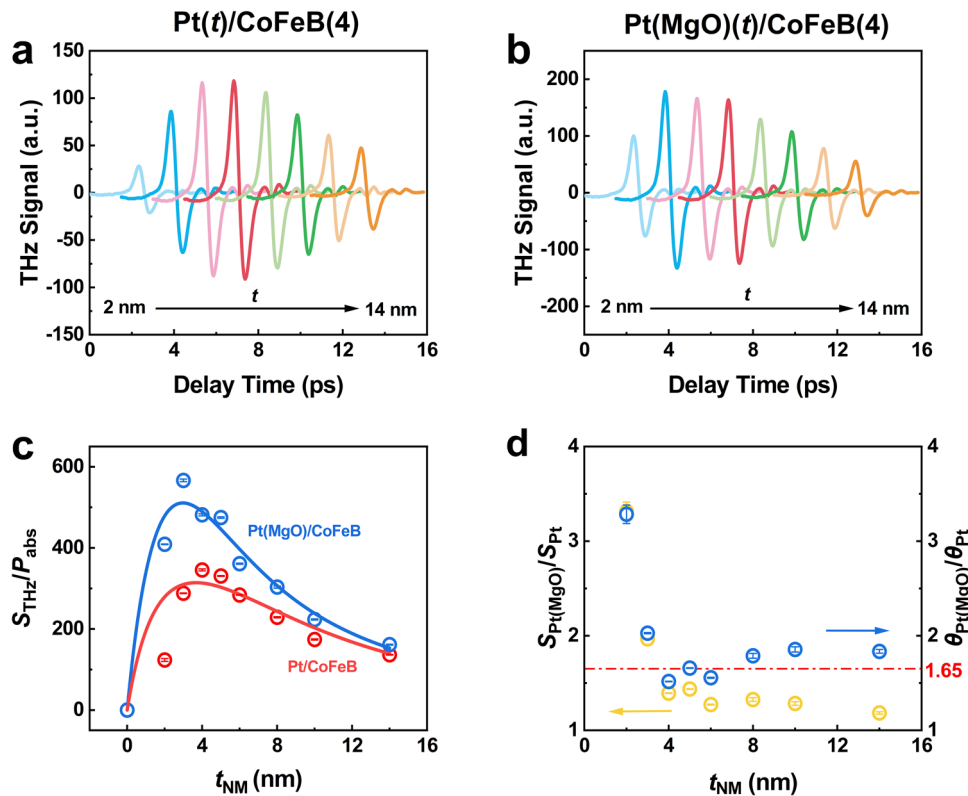


Fig. 3 Spin diffusion length and relative spin Hall angle of $\text{Pt}_{0.93}(\text{MgO})_{0.07}$. THz pulses emitted from the sample were measured under different thickness of **a** Pt, **b** $\text{Pt}_{0.93}(\text{MgO})_{0.07}$ ($t = 2, 3, 4, 5, 6, 8, 10, 14$ nm). **c** The relation of $S_{\text{THz}}/P_{\text{abs}}$ with t_{NM} . The grey circles represent $\text{Pt}_{0.93}(\text{MgO})_{0.07}/\text{CoFeB}$ samples and the red squares represent Pt/CoFeB samples. The solid lines represent fitting results. The error bars in **c** are due to the deviation of the mean values of multiple measurements. **d** Dependence of the enhancement ratio (yellow diamond) and relative spin Hall angle (blue circles) on the NM layer thickness. When t is greater than 4 nm, the relative spin Hall Angle is around 1.65. The error bars in **d** are due to the deviation of the fitting of λ_s of Eq. (1).

its maximum value at $t_{\text{Pt}} = 5$ nm. In a typical FM/NM heterostructure, such thickness dependence is determined by the spin diffusion length (λ_s) of NM materials.

To obtain a quantitative analysis of the effect of MgO doping on the spin diffusion length, we used a theoretical model to fit the experimental results as shown in Fig. 3c (The details of the fitting method is discussed in the Supplementary Note 6.). An approximate theoretical formula for the amplitude of the terahertz electric field can be expressed as^{25,53}

$$E_{\text{THz}} \propto \frac{AZ_0 P_{\text{abs}} T \theta_{\text{SHE}} \lambda_s \tanh\left(\frac{t_{\text{NM}}}{2\lambda_s}\right)}{(t_{\text{NM}} + t_{\text{FM}})(n_1 + n_2 + Z_0 \int_0^{t_{\text{NM}} + t_{\text{FM}}} \sigma(z) dz)} \quad (1)$$

Where $Z_0 = 377 \Omega$, is the impedance of the vacuum, $n_1 = 1$ and $n_2 = 1.98$ are the refractive index of air, and the SiO_2 substrate (n_2 was obtained by THz transmission spectroscopy), respectively, θ_{SHE} is the spin Hall angle of NM material, λ_s is the spin diffusion length of NM layer, A is an insignificant parameter that depends on the excitation of the sample by the incident laser, t is the films thickness, P_{abs} is the absorption of the laser power by the sample [Supplementary Note 7], σ is the terahertz conductivity [Supplementary Note 8], T is the spin transparency from the FM layer to the NM layer. The doped and reference samples' spin diffusion lengths are fitted as $\lambda_{\text{Pt}(\text{MgO})} = 2 \pm 0.2$ nm and $\lambda_{\text{Pt}} = 4 \pm 0.2$ nm for the doped sample and reference samples, respectively. The spin diffusion length we obtained for Pt is comparable to that reported in earlier works^{53,54}. However, the spin-diffusion length of $\text{Pt}_{1-x}(\text{MgO})_x$ has rarely been studied, and in most works, the spin-diffusion length was approximated by the electrical conductivity^{45,55}. In addition, we can see from Fig. 3c that the fitted curves deviate from the experimental data in the range of thin

NM layers. We attribute this phenomenon to the neglect of interfacial spin loss. Interfacial spin resistance and spin memory loss occur at the interface of FM and NM films due to resistive mismatch and spin scattering, which causes spin loss²⁷. The reduction in the spin-diffusion length of $\text{Pt}_{0.93}(\text{MgO})_{0.07}$ relative to Pt is attributed to the doping of MgO, which enhances the spin flip of polarized electrons. Another key parameter in Eq. (1) that affects terahertz emission is spin Hall angle, θ_{SHE} . To obtain the relative spin Hall angle of $\text{Pt}_{0.93}(\text{MgO})_{0.07}$ with respect to Pt, we assume that the two structures have the same spin transparency T and A . We used the spin diffusion length that fit above and compared the THz signals generated by the two kinds of structures (shown in Fig. 3d by yellow diamond) with Eq. (1) to obtain the relative spin Hall angle $\theta_{\text{rela}} = \theta_{\text{Pt}(\text{MgO})}/\theta_{\text{Pt}}$ ($\theta_{\text{Pt}(\text{MgO})}$ and θ_{Pt} represent spin Hall angles for Pt(MgO) and Pt, respectively)⁵⁵. The computed relative spin Hall angle is NM film thickness dependent, and the relationship between θ_{rela} and t_{NM} is shown in Fig. 3d (blue circles). We find that $\text{Pt}_{0.93}(\text{MgO})_{0.07}$ exhibits an almost stable and constant relative spin Hall angle of about 1.65 ± 0.20 (± 0.20 represents that the calculated spin Hall Angle at different Pt thicknesses fluctuates in the range of 0.20 around 1.65, as shown in Fig. 3d) in the thick NM thickness range ($t \gg \lambda_{\text{Pt}}$), while shows a larger relative spin Hall angle in the thin NM thickness range, particularly at $t = 2$ nm, where the θ_{rela} of $\text{Pt}_{0.93}(\text{MgO})_{0.07}$ approaches 3.5.

The origin of high-intensity THz signal. Considering the spin Hall effect (SHE) based on spin-orbit interactions can be divided into intrinsic and extrinsic mechanisms (side jump and skew scattering), the spin Hall resistivity and spin Hall angle can be expressed

as $\rho_{SH} = \sigma_{SH}^{int} \rho_{xx}^2 + \rho_{SH}^{imp}$ and $\theta_{SH} = \rho_{SH} / \rho_{xx}$, where ρ_{SH} is the total spin Hall resistivity, σ_{SH}^{int} is the intrinsic spin Hall conductivity of Pt, ρ_{xx} is the longitudinal electrical resistivity, and ρ_{SH}^{imp} is the extrinsic spin Hall resistivity induced by the MgO intersite impurities⁵⁶. Typically, the σ_{SH}^{int} of Pt originates from the intrinsic SHE determined by the topology of band structure, which for simple fcc metals is only dependent on the long-range crystal structure⁵⁷. Figure 1c depicts the XRD $\theta-2\theta$ patterns of $Pt_{1-x}(MgO)_x$ single layer. As x rises, Pt still exhibits robust long-range fcc order as x increases, indicating negligible modification in intrinsic σ_{SH}^{int} . However, a giant variation in σ_{SH}^{int} can be brought via tuning the scattering from the finely dispersed MgO intersite impurities, which are built on the basis of high doping concentration⁴⁵. The variation in the σ_{SH}^{int} of our samples is insignificant since the concentration of MgO in Pt in our study is low, as evidenced by the weak change in intensity and full width at half maximum in the XRD patterns (Fig. 1c). Supplementary Fig. 8b depicts the resistance of a single NM layer, the room temperature resistivities of the doped and reference samples are $\rho_{Pt(MgO)} = 54 \mu\Omega \text{ cm}$ and $\rho_{Pt} = 36 \mu\Omega \text{ cm}$, respectively. The introduction of MgO forms a large number of intersite impurities to concentrate electrons and create an internal electric field, thus increasing the resistance. Theoretically, the intrinsic contribution dominates the SHE of Pt in the dirty-metal regime (ρ_{xx} larger than $\sim 30 \mu\Omega \cdot \text{cm}$) while the extrinsic contributions become dominant in the ultraclean regime⁵⁸. Therefore, the variation of ρ_{SH}^{imp} should be small. On the other hand, the contribution of skew scattering should scale inversely with the residual resistivity ratio ($RRR = \rho_{xx} / \rho_{xx,0}$, where $\rho_{xx,0}$ is the low-temperature resistivity)⁵⁹, the RRR of the doped and reference samples are 1.12 and 1.16, respectively, the slight change indicating this contribution is negligible in our samples. And side jump should also give rise to a linear contribution in θ_{SHE} with respect to ρ_{xx} like intrinsic mechanism⁴³. Obviously, we can obtain that the spin Hall angle is approximately proportional to the longitudinal electrical resistivity ($\theta_{SHE} \propto \rho_{xx}$) in our low-MgO doping samples. The relative resistance at room temperature $\rho_{rela} = \rho_{Pt(MgO)} / \rho_{Pt} = 1.50$, in excellent agreement with the relative spin Hall angle ($\theta_{rela} = 1.65 \pm 0.20$) as shown in Fig. 3d. Although continuing to increase the doping concentration will further increase the resistance, the carrier lifetime rapidly decreases, thereby reducing the intrinsic spin Hall conductance and shortening the spin diffusion length, resulting in a weakened THz signal. By now we infer that the competing relationship of enhanced bulk spin Hall angle, which is caused by the increase in resistance, and decreased spin diffusion length can be used to explain the influence of THz signal due to low-MgO doping. According to this extrapolation, we should get a stable spin Hall angle increase rather than a NM film thickness-dependent relative spin Hall angle. And the resistance change we measured is not large enough to bring about such a large signal enhancement in the thin NM layer thickness range. Therefore, in addition to the bulk-like effects, the interfacial contributions also need to be considered in the process of THz emission from STEs^{47,60}.

To evaluate whether the FM/NM interface plays a role in the enhancement phenomenon and investigate the relationship of $\theta_{rela} - t_{NM}$, we study samples with varied interlayer thicknesses using Cu as the interlayer. Cu is suitable as an interlayer due to its long spin diffusion length and negligibly small ISHE. As we can see in Fig. 4, the introduction of the Cu interlayer changes the THz intensity of all samples. Many previous works^{53,61} have reported that the Cu interlayer suppresses the transmission of spin current and thus reduces the THz signal, but in our experiments, the introduction of the Cu interlayer has a different effect for samples with different Pt layer thicknesses. In the doped samples, the Cu interlayer attenuates the THz signal, but in the reference sample, the THz signal is enhanced due to the

introduction of Cu at $t_{Pt} = 2$ and 3 nm (Fig. 4a, b). This phenomenon may be caused by the variation of pump laser absorbance and the ISHE of Cu itself. However, the experimental results prove that these cases are negligible (Supplementary Note 9 and Supplementary Note 10).

Then we turn our attention to the NM/FM interface, Pt/Cu(t_{Cu})/CoFeB and Pt(MgO)/Cu(t_{Cu})/CoFeB exhibit different Cu thickness dependence in thin NM layer thickness range (Fig. 4a, b) implying that the interface of doped sample and reference sample is different and that the bulk property of Pt(MgO) is not the only reason for terahertz signal enhancement. The EDS mapping image (Fig. 1d) shows that the MgO impurities are not only uniformly distributed in the Pt, but also contain a large amount of Mg elements within the CoFeB layer, which comes partly from the penetration of the MgO protective layer and partly from the penetration of the MgO impurities in the Pt, having a modification on the Pt(MgO)/CoFeB interface. In the thick NM layer region, Fig. 4c, d exhibit identical Cu thickness dependence, indicating that interfacial effects can be ignored. In another experiment, we replaced Cu with MgO as an interlayer. The THz signals generated from Pt(3)/MgO(1)/CoFeB (4) and Pt_{0.93}(MgO)_{0.07}(3)/MgO(1)/CoFeB(4) are shown in Fig. 4e. The insertion of MgO severely attenuates the spin current, causing the signal to decrease rapidly. Interestingly, we found that the signals of the doped sample and the reference sample were almost the same when a 1 nm MgO interlayer was inserted. The insertion of MgO destroys the FM/NM interface on one hand, while the diffusion of MgO from the interlayer into the NM layer causes Pt to form Pt_{1-x}(MgO)_x, both of which make the reference sample and the doped sample form similar structural compositions thus making the signals similar. Therefore, we propose the following hypothesis: The role of bulk and interface differs significantly in NM layers of varying thickness.

Figure 5a depicts the generation of charge current in a thin NM layer, where the bulk effect (J_{c1}) is weak due to restricted spin diffusion, whereas the interface has a large contribution (J_{c2}). The lower panel of Fig. 5a shows that in the doped sample, both interfacial and bulk effects are considerably amplified, increasing final charge current. The interface has been reported to contribute considerably to the ISHE, ascribed to impurity skew scattering⁴⁷ at the interface. MgO molecule diffuses into the Pt(MgO)/CoFeB interface region and the interior of CoFeB, amplifying the skew scattering of spin-polarized electrons at the interface and in CoFeB as illustrated in the lower panel of Fig. 5a, resulting in terahertz signal enhancement. This explains the doped samples' notably high relative spin Hall angles for thin NM layers in our finding. Introducing the Cu interlayer disrupts the Pt(MgO)/CoFeB interface and decreases the impact of interfacial skew scattering, decreasing the THz signal. While the THz signal in Pt/Cu/CoFeB is visibly enhanced compared to Pt/CoFeB, this phenomenon may be due to the characteristics of distinct interfaces, such as interface-caused enhancement of ISHE in thin Pt range⁶² or IREE induced at the Pt/Cu interface⁶³. The scenario differs when the NM layer thickness is substantial, as seen in Fig. 5b. Because the NM layer thickness is greater than the spin diffusion length in this situation, the spin current may flow sufficiently into NM to provide a large charge current, and the effect produced by the interface can be ignored in terms of the bulk effect. Considering only the enhanced bulk spin Hall angle and the reduced spin diffusion length without the interface effect coincides well with the experimental data, which show that the signals of the doped sample and the reference sample converge at thick NM and have identical Cu thickness dependency. In addition, as shown in Supplementary Note 11, various enhancement phenomena arise in different Pt_{1-x}(MgO)_x/FM systems, indicating that the interface plays a non-negligible role

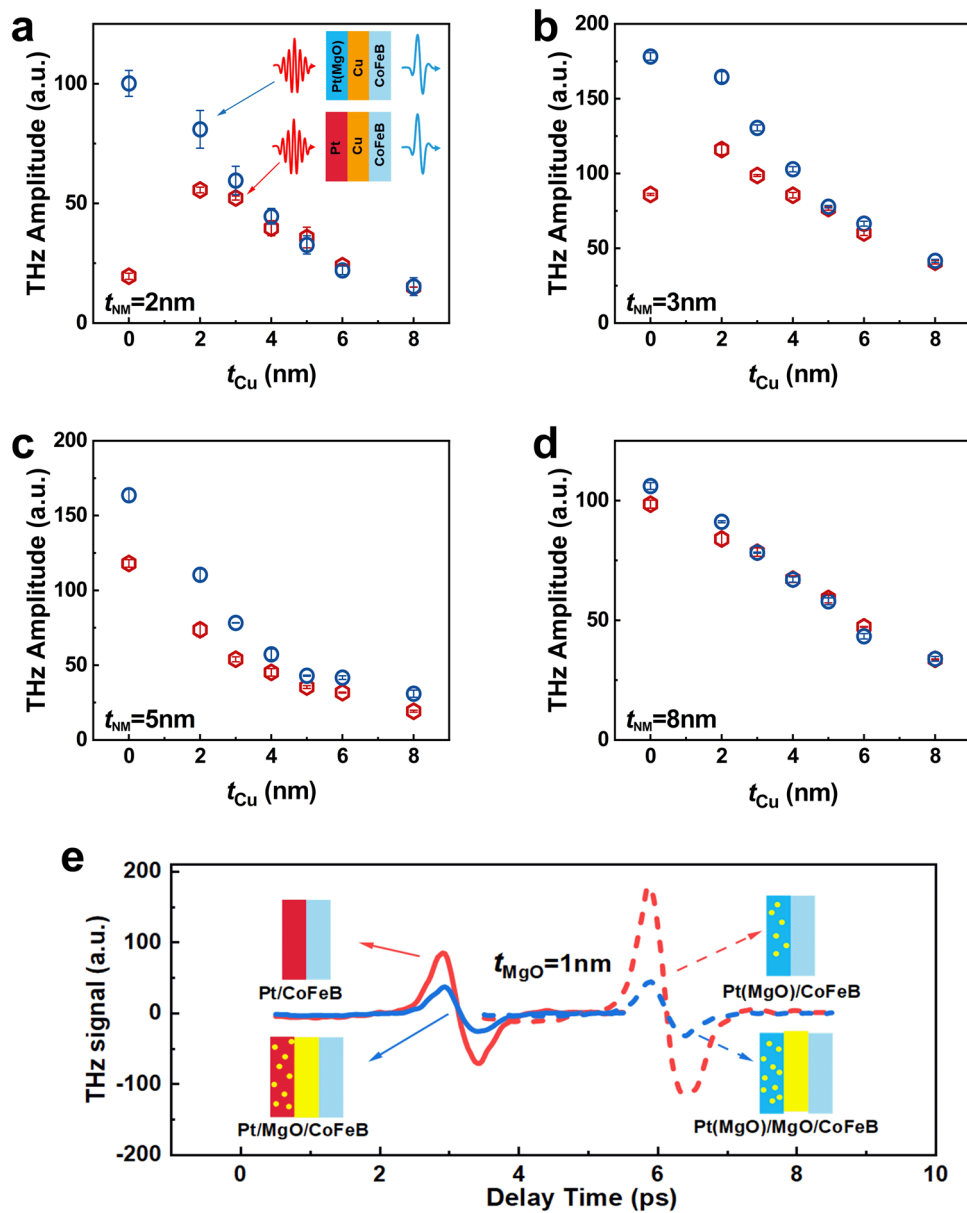


Fig. 4 The effect of interlayer on the amplitude of THz signal. Cu thickness dependence of the THz amplitude from Pt_{0.93}(MgO)_{0.07}/CoFeB (blue circles) and Pt/CoFeB (red squares) with different thickness of NM **a** NM(2)/Cu(*t*)/CoFeB(4), **b** NM(3)/Cu(*t*)/CoFeB(4), **c** NM(5)/Cu(*t*)/CoFeB(4), **d** NM(8)/Cu(*t*)/CoFeB(4). The error bars in **a**, **b**, **c**, and **d** are due to deviation from the mean values of multiple measurements. **e** THz emission signals of Pt(3)/CoFeB(4) (red solid line), Pt_{0.93}(MgO)_{0.07}(3)/CoFeB(4) (red dotted line), Pt(3)/MgO(1)/CoFeB(4) (blue solid line) and Pt_{0.93}(MgO)_{0.07}(3)/MgO(1)/CoFeB(4) (blue dotted line) samples.

in THz signal enhancement. This interface effect is often overlooked in much of the works based on electrical methods^{45,46}.

The 2 nm Cu interlayer is sufficient to disrupt the NM/FM interface. To separate the bulk and interfacial contributions, we approximate $E_{\text{bulk}} + E_{\text{interface}} = E_{\text{Pt(MgO)/CoFeB}} - E_{\text{Pt/CoFeB}}$, $E_{\text{bulk}} = E_{\text{Pt(MgO)/Cu(2)/CoFeB}} - E_{\text{Pt/CoFeB}}$, so $E_{\text{interface}} = E_{\text{Pt(MgO)/CoFeB}} - E_{\text{Pt(MgO)/Cu(2)/CoFeB}}$ (Fig. 5c, d). We find that the interfacial effect is non-negligible at thin NM layers. Here, we ignored the attenuating effect of Cu on the spin current in Pt(MgO)/Cu(2)/CoFeB and the probable enhancing effect of the Pt_{0.93}(MgO)_{0.07}/Cu interface, which would greatly underestimate the role of the interface in our calculations. However, more detailed studies can be done for a further understanding of the enhancement. In addition, we conducted experiments on W_{1-x}(MgO)_x and obtained similar results to Pt (Supplementary Note 12). This result shows that our method is somewhat universal.

Conclusions

In summary, we propose a high-intensity spintronic terahertz emitter with a simple FM/NM bilayer structure by doping MgO impurity into Pt as the NM material and demonstrate THz signal enhancement compared to the undoped sample. An optimized Pt_{0.93}(MgO)_{0.07}/CoFeB structure reaches a 200% intensity compared to Pt/CoFeB and approaches the signal of 500 μ m ZnTe crystal. The mechanism of THz emission from the doped sample is still ISHE. We fitted the experimental results to the spin-diffusion model and found that MgO doping shortened the spin-diffusion length. A thickness-dependent relative spin Hall angle was obtained by further analysis. We attribute the enhancement of the THz signal to increased bulk spin Hall angle and interfacial skew scattering by MgO impurities. Additionally, we separated the effect of interfacial contribution and bulk contribution using the interlayer experiment. And we find that the Cu interlayer has

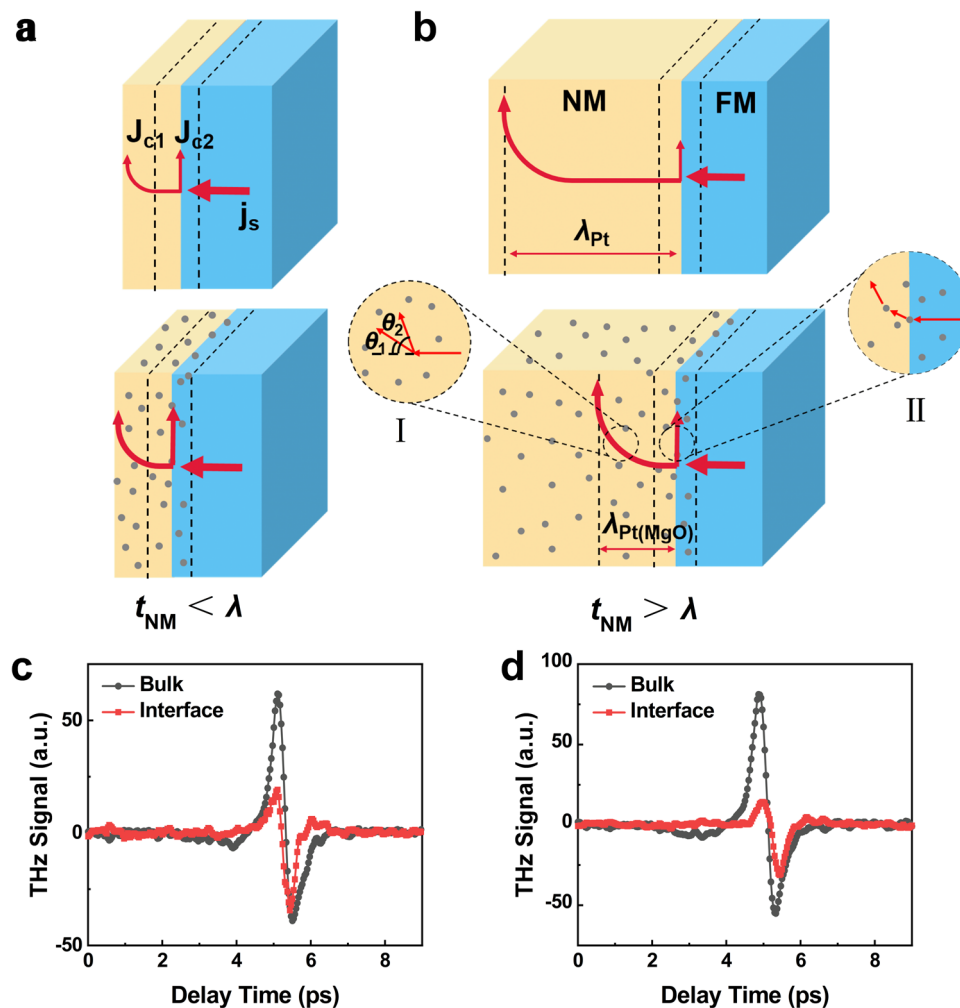


Fig. 5 Separation of bulk effect and interface effect. Schematic diagram of terahertz enhancement by MgO doping at different NM thicknesses. **a** $t < \lambda$, **b** $t \geq \lambda$. j_s , j_{c1} , and j_{c2} represent the spin current, the charge current generated in the bulk, and the charge current generated at the interface, respectively. The spin diffusion length of Pt and Pt(MgO) is represented by λ_{Pt} and $\lambda_{Pt(MgO)}$. The enlarged figure I represents that the bulk spin Hall angle increases from θ_1 to θ_2 after doping MgO. The enlarged figure II represents the interface skew scattering contribution caused by MgO molecules. Separation of interfacial (red squares) and bulk (black circles) enhancement effects in Pt_{0.93}(MgO)_{0.07}(t)/CoFeB **c** $t = 2$ nm, **d** $t = 3$ nm.

different effects on different thicknesses of Pt. Our findings also reveal the role of the interface in the THz emission of spintronics sources. Furthermore, stronger THz signals may be obtained by optimizing the doping concentration, changing the main NM material, changing the doping material, or combining with the NM/FM/NM trilayer or the multilayer structures, which proposes a promising route to enhance the performance of THz optoelectronic devices.

Methods

Sample fabrication. The Pt_{1-x}(MgO)_x/CoFeB/MgO stack with different MgO content was grown on a 500- μ m-thick 5×5 mm² SiO₂ substrate by magnetron sputtering. The Pt_{1-x}(MgO)_x layer was co-sputtered from a Pt and MgO target. The speed of film growth was measured by X-ray reflection (XRR) as shown in Supplementary Note 13. The content of MgO was controlled by fixing the sputtering power of the Pt target and changing the sputtering power of the MgO target. The content of MgO and elemental valence state were determined by x-ray photoemission spectroscopy (XPS). MgO capping was used as a protective layer to prevent sample oxidation. Element content and distribution were determined by cross-sectional energy dispersive X-ray spectroscopy (EDS).

Microscopic topography experiments. The cross-sectional morphology of the stack and the surface morphology of the Pt_{1-x}(MgO)_x single layers were measured by cross-sectional transmission electron microscopy (TEM) and atomic force microscopy (AFM), respectively.

THz emission spectroscopy measurement. A static external magnetic field of 700 Oe was applied parallel to the sample surface along the x-axis to keep the CoFeB saturated magnetization. We used a Ti: Sapphire laser with a pulse width of 35 fs, a center wavelength of 800 nm, and a repetition rate of 1 kHz. The exciting beam was focused on the sample with a spot size of about 3 mm in diameter and an average pump fluence of 720 μ J cm⁻². In general, the laser can be incident from the substrate side or the sample side. But in the paper, the laser was incident from the substrate side to avoid undesired THz absorption by the substrate unless otherwise stated for convenience. The THz emission was collected by a pair of parabolic mirrors and then measured using electro-optic sampling in a 500- μ m-thick (110)-oriented ZnTe crystal. All the measurements were conducted at room temperature in dry air gas to prevent water vapor absorption in the ambient air. (The details of the setup are shown in Supplementary Note 4).

Vibrating sample magnetometry (VSM) measurements. The sample magnetization was measured by a superconducting quantum interference device-vibrating sample magnetometry (VSM) at room temperature.

Data availability

All data presented in this study are available from the corresponding authors upon reasonable request.

Received: 4 May 2023; Accepted: 21 September 2023;

Published online: 29 September 2023

References

- Ferguson, B. & Zhang, X. C. Materials for terahertz science and technology. *Nat. Mater.* **1**, 26–33 (2002).
- Lee, A. J., Spence, D. J. & Pask, H. M. Terahertz sources based on stimulated polariton scattering. *Prog. Quantum Electron.* **71**, 100254 (2020).
- Ho, L., Pepper, M. & Taday, P. Terahertz Spectroscopy: Signatures and fingerprints. *Nat. Photonics* **2**, 541–543 (2008).
- Koenig, S. et al. Wireless sub-THz communication system with high data rate. *Nat. Photonics* **7**, 977–981 (2013).
- Mittleman, D. M. Perspective: Terahertz science and technology. *J. Appl. Phys.* **122**, 230901 (2017).
- Dikmelik, Y., Spicer, J. B., Fitch, M. J. & Oslander, R. Effects of surface roughness on reflection spectra obtained by terahertz time-domain spectroscopy. *Opt. Lett.* **31**, 3653–3655 (2006).
- Nguyen, D. T. et al. A method for non-destructive determination of cocoa bean fermentation levels based on terahertz hyperspectral imaging. *Int. J. Food Microbiol.* **365**, 109537 (2022).
- El-Shenawee, M., Vohra, N., Bowman, T. & Bailey, K. Cancer detection in excised breast tumors using terahertz imaging and spectroscopy. *Biomed. Spectrosc. Imaging* **8**, 1–9 (2019).
- Pickwell, E. & Wallace, V. P. Biomedical applications of terahertz technology. *J. Phys. D.* **39**, R301–R310 (2006).
- Chen, S. C. et al. Ghost spintronic THz-emitter-array microscope. *Light Sci. Appl.* **9**, 99 (2020).
- Kolbel, J., Li, Q., Threlfall, T. L. & Zeitler, J. A. Measuring Solute Concentration with Terahertz Time-Domain Spectroscopy in Single and Multiphase Systems. *Anal. Chem.* **94**, 1713–1716 (2022).
- Luo, Y. et al. Nanoscale terahertz STM imaging of a metal surface. *Phys. Rev. B* **102**, 205417 (2020).
- Lepeshov, S., Gorodetsky, A., Krasnok, A., Rafailov, E. & Belov, P. Enhancement of terahertz photoconductive antenna operation by optical nanoantennas. *Laser Photonics Rev.* **11**, 1600199 (2017).
- Yardimci, N. T. & Jarrahi, M. Nanostructure-Enhanced Photoconductive Terahertz Emission and Detection. *Small* **14**, e1802437 (2018).
- Jang, D. & Kim, K. Y. Multicycle terahertz pulse generation by optical rectification in LiNbO₃, LiTaO₃, and BBO crystals. *Opt. Express* **28**, 21220–21235 (2020).
- Rice, A. et al. Terahertz Optical Rectification from (110) Zinblend Crystals. *Appl. Phys. Lett.* **64**, 1324–1326 (1994).
- Löffler, T., Hahn, T., Thomson, M., Jacob, F. & Roskos, H. G. Large-area electro-optic ZnTe terahertz emitters. *Opt. Express* **13**, 5353–5362 (2005).
- Xu, S. S. et al. Generation of Terahertz Radiation by Optical Rectification Using Femtosecond Bessel Beam. *IEEE J. Sel. Top. Quantum Electron.* **23**, 1–6 (2017).
- Yang, K. H., Richards, P. L. & Shen, Y. R. Generation of Far-Infrared Radiation by Picosecond Light Pulses in LiNbO₃. *Appl. Phys. Lett.* **19**, 320 (1971).
- Feng, Z. et al. Spintronic terahertz emitter. *J. Appl. Phys.* **129**, 010901 (2021).
- Fulop, J. A., Tzortzakis, S. & Kampfrath, T. Laser-Driven Strong-Field Terahertz Sources. *Adv. Opt. Mater.* **8**, 1900681 (2019).
- Seifert, T. S., Cheng, L., Wei, Z. X., Kampfrath, T. & Qi, J. B. Spintronic sources of ultrashort terahertz electromagnetic pulses. *Appl. Phys. Lett.* **120**, 180401 (2022).
- Jungfleisch, M. B. et al. Control of Terahertz Emission by Ultrafast Spin-Charge Current Conversion at Rashba Interfaces. *Phys. Rev. Lett.* **120**, 207207 (2018).
- Kampfrath, T. et al. Terahertz spin current pulses controlled by magnetic heterostructures. *Nat. Nanotechnol.* **8**, 256–260 (2013).
- Seifert, T. et al. Efficient metallic spintronic emitters of ultrabroadband terahertz radiation. *Nat. Photonics* **10**, 483–488 (2016).
- Kumar, N., Hendrikx, R. W. A., Adam, A. J. L. & Planken, P. C. M. Thickness dependent terahertz emission from cobalt thin films. *Opt. Express* **23**, 14252–14262 (2015).
- Qiu, H. S. et al. Layer thickness dependence of the terahertz emission based on spin current in ferromagnetic heterostructures. *Opt. Express* **26**, 15247–15254 (2018).
- Wu, Y. et al. High-Performance THz Emitters Based on Ferromagnetic/Nonmagnetic Heterostructures. *Adv. Mater.* **29**, 1603031 (2017).
- Scheuer, L. et al. THz emission from Fe/Pt spintronic emitters with L10-FePt alloyed interface. *Science* **25**, 104319 (2022).
- Nandi, U. et al. Antenna-coupled spintronic terahertz emitters driven by a 1550nm femtosecond laser oscillator. *Appl. Phys. Lett.* **115**, 022405 (2019).
- Liu, C. Q. et al. Active spintronic-metasurface terahertz emitters with tunable chirality. *Adv. Photonics* **3**, 056002 (2021).
- Schlauderer, S. et al. Temporal and spectral fingerprints of ultrafast all-coherent spin switching. *Nature* **569**, 383–387 (2019).
- Li, X. et al. Terahertz field-induced ferroelectricity in quantum paraelectric SrTiO₃. *Science* **364**, 1079–1082 (2019).
- Cocker, T. L., Peller, D., Yu, P., Repp, J. & Huber, R. Tracking the ultrafast motion of a single molecule by femtosecond orbital imaging. *Nature* **539**, 263–267 (2016).
- Liu, L. Q. et al. Spin-Torque Switching with the Giant Spin Hall Effect of Tantalum. *Science* **336**, 555–558 (2012).
- Pai, C. F. et al. Spin transfer torque devices utilizing the giant spin Hall effect of tungsten. *Appl. Phys. Lett.* **101**, 122404 (2012).
- Wang, L. et al. Giant Room Temperature Interface Spin Hall and Inverse Spin Hall Effects. *Phys. Rev. Lett.* **116**, 196602 (2016).
- Wu, X. J. et al. Antiferromagnetic-Ferromagnetic Heterostructure- Based Field-Free Terahertz Emitters. *Adv. Mater.* **34**, 2204373 (2022).
- Vetter, E. et al. Observation of carrier concentration dependent spintronic terahertz emission from n-GaN/NiFe heterostructures. *Appl. Phys. Lett.* **117**, 093502 (2020).
- Fang, Z. J. et al. Nonlinear terahertz emission in the three-dimensional topological insulator Bi₂Te₃ by terahertz emission spectroscopy. *Appl. Phys. Lett.* **115**, 191102 (2019).
- Wang, X. B. et al. Ultrafast Spin-to-Charge Conversion at the Surface of Topological Insulator Thin Films. *Adv. Mater.* **30**, 1802356 (2018).
- Zhu, L. J., Zhu, L. J., Shi, S. J., Ralph, D. C. & Buhrman, R. A. Energy-Efficient Ultrafast SOT-MRAMs Based on Low-Resistivity Spin Hall Metal Au_{0.25}Pt_{0.75}. *Adv. Electron. Mater.* **6**, 1901131 (2020).
- Ramaswamy, R. et al. Extrinsic Spin Hall Effect in Cu_{1-x}Pt_x. *Phys. Rev. Appl.* **8**, 024034 (2017).
- Wang, P. et al. Giant Spin Hall Effect and Spin-Orbit Torques in 5d Transition Metal-Aluminum Alloys from Extrinsic Scattering. *Adv. Mater.* **34**, 2109406 (2022).
- Zhu, L. J., Zhu, L. J., Sui, M. L., Ralph, D. C. & Buhrman, R. A. Variation of the giant intrinsic spin Hall conductivity of Pt with carrier lifetime. *Sci. Adv.* **5**, eaav8025 (2019).
- Xu, X. K. et al. Giant Extrinsic Spin Hall Effect in Platinum-Titanium Oxide Nanocomposite Films. *Adv. Sci.* **9**, 2105726 (2022).
- Gueckstock, O. et al. Terahertz Spin-to-Charge Conversion by Interfacial Skew Scattering in Metallic Bilayers. *Adv. Mater.* **33**, 2006281 (2021).
- An, H., Kanno, Y., Asami, A. & Ando, K. Giant spin-torque generation by heavily oxidized Pt. *Phys. Rev. B* **98**, 014401 (2018).
- Svintitskiy, D. A. et al. Highly Oxidized Platinum Nanoparticles Prepared through Radio-Frequency Sputtering: Thermal Stability and Reaction Probability towards CO. *ChemPhysChem* **16**, 3318–3324 (2015).
- Seyama, H. & Soma, M. X-Ray Photoelectron Spectroscopic Study of Montmorillonite Containing Exchangeable Divalent-Cations. *J. Chem. Soc. Farad. T* **1** **80**, 237–248 (1984).
- Wagner, C. D., Zlatko, D. A. & Raymond, R. H. Use of the Oxygen K_{LL} Auger Lines in Identification of Surface Chemical-States by Electron-Spectroscopy for Chemical-Analysis. *Anal. Chem.* **52**, 1445–1451 (1980).
- Zhou, C. et al. Broadband Terahertz Generation via the Interface Inverse Rashba-Edelstein Effect. *Phys. Rev. Lett.* **121**, 086801 (2018).
- Zhang, H. et al. Laser pulse induced efficient terahertz emission from Co/Al heterostructures. *Phys. Rev. B* **102**, 024435 (2020).
- Kondou, K., Sukegawa, H., Mitani, S., Tsukagoshi, K. & Kasai, S. Evaluation of Spin Hall Angle and Spin Diffusion Length by Using Spin Current-Induced Ferromagnetic Resonance. *Appl. Phys. Express* **5**, 073002 (2012).
- Meinert, M. et al. High-Throughput Techniques for Measuring the Spin Hall Effect. *Phys. Rev. Appl.* **14**, 064011 (2020).
- Isasa, M., Villamor, E., Hueso, L. E., Gradhand, M. & Casanova, F. Temperature dependence of spin diffusion length and spin Hall angle in Au and Pt. *Phys. Rev. B* **91**, 024402 (2015).
- Zhu, L. J., Ralph, D. C. & Buhrman, R. A. Spin-Orbit Torques in Heavy-Metal-Ferromagnet Bilayers with Varying Strengths of Interfacial Spin-Orbit Coupling. *Phys. Rev. Lett.* **122**, 077201 (2019).

58. Vignale, G. Ten Years of Spin Hall Effect. *J. Supercond. Nov. Magn.* **23**, 3–10 (2010).
59. Sagasta E. et al. Tuning the spin Hall effect of Pt from the moderately dirty to the superclean regime. *Phys. Rev. B* **94**, 060412 (2016).
60. Kumar, S. & Kumar, S. Large interfacial contribution to ultrafast THz emission by inverse spin Hall effect in CoFeB/Ta heterostructure. *Science* **25**, 104718 (2022).
61. Seifert, T. S. et al. Terahertz spectroscopy for all-optical spintronic characterization of the spin-Hall-effect metals Pt, W and Cu₈₀Ir₂₀. *J. Phys. D: Appl. Phys.* **51**, 364003 (2018).
62. Zhu, T., Chang, F. F. & Zhan, X. Z. Interface induced enhancement of inverse spin Hall voltage in NiFe/Pt bilayers capped by MgO layer. *J. Phys. Condens.* **31**, 285801 (2019).
63. Yu, R. et al. Fingerprint of the inverse Rashba-Edelstein effect at heavy-metal/Cu interfaces. *Phys. Rev. B* **102**, 144415 (2020).

Acknowledgements

This work was supported by Key Research and Development Program of Anhui Province (No. 2022a05020051), the National Natural Science Foundation of China (Grant No. 51627901), National Key R&D Program of China (2020YFA0710100), the Anhui Initiative in Quantum Information Technologies (AHY100000), and Key Research and Development Program of Anhui Province, No. 202104A05020012.

Author contributions

The study was performed under the supervision of QH and YL. And YW fabricated samples, conducted terahertz emission measurements, and performed terahertz time-domain spectroscopy measurements with the help of HC and ZL, WL performed structural and morphological measurements of samples and electrical tests with the help of ZC, JH, BX, and JY. And YW performed data analysis with the help of HH, JW, ZF, QH and YL. And YW wrote the paper with the help of all authors.

Competing interests

The authors declare no competing interests.

Additional information

Supplementary information The online version contains supplementary material available at <https://doi.org/10.1038/s42005-023-01402-x>.

Correspondence and requests for materials should be addressed to Qiuping Huang or Yalin Lu.

Peer review information *Communications Physics* thanks Caihong Zhang and the other, anonymous, reviewer(s) for their contribution to the peer review of this work.

Reprints and permission information is available at <http://www.nature.com/reprints>

Publisher's note Springer Nature remains neutral with regard to jurisdictional claims in published maps and institutional affiliations.



Open Access This article is licensed under a Creative Commons Attribution 4.0 International License, which permits use, sharing,

adaptation, distribution and reproduction in any medium or format, as long as you give appropriate credit to the original author(s) and the source, provide a link to the Creative Commons licence, and indicate if changes were made. The images or other third party material in this article are included in the article's Creative Commons licence, unless indicated otherwise in a credit line to the material. If material is not included in the article's Creative Commons licence and your intended use is not permitted by statutory regulation or exceeds the permitted use, you will need to obtain permission directly from the copyright holder. To view a copy of this licence, visit <http://creativecommons.org/licenses/by/4.0/>.

© The Author(s) 2023